INSTABILITIES AND MIXING IN SN 1993J

KOHICHI IWAMOTO, TIMOTHY R. YOUNG, NAOHITO NAKASATO, TOSHIKAZU SHIGEYAMA,
AND KEN'ICHI NOMOTO
Department of Astronomy, School of Science, University of Tokyo, Bunkyo-ku, Tokyo 113, Japan

IZUMI HACHISU
Department of Earth Science and Astronomy, College of Arts and Sciences, University of Tokyo, Meguro-ku, Tokyo 153, Japan

AND

HIDEYUKI SAIO
Department of Astronomy, Faculty of Science, Tohoku University, Sendai 980-01, Japan
Received 1996 May 20; accepted 1996 October 1

ABSTRACT

Rayleigh-Taylor (R-T) instabilities in the explosion of SN 1993J are investigated by means of two-dimensional hydrodynamical simulations. It is found that the extent of mixing is sensitive to the progenitor's core mass and the envelope mass. Because the helium core mass (3–4 $M_\odot$) is smaller than that of SN 1987A, R-T instabilities at the He/C+O interface develop to induce a large-scale mixing in the helium core, while the instability is relatively weak at the H/He interface as a result of the small envelope mass. The predicted abundance distributions, in particular the extent of the ^{56}Ni mixing, are compared with those required in modeling the bolometric light curve and the late-time optical spectra. These comparisons provide significant constraints on the masses of the helium core and the envelope of the progenitor of SN 1993J.

Subject headings: hydrodynamics — instabilities — stars: interiors — supernovae: individual (SN 1993J)

1. INTRODUCTION

SN 1993J has been identified as a Type IIb supernova (SN IIb) from the spectral changes that show growing features of helium and oxygen, and from the optical light curve that shows double peaks (Wheeler & Filippenko 1995; Baron, Hauschildt, & Young 1995 for reviews and references therein). These features are distinct from those of previously known Type II supernovae (SNe II). It was obvious that the peculiar light curve of SN 1993J cannot be accounted for by an explosion of an ordinary red supergiant with a massive hydrogen-rich envelope, which produces a light curve of a SN II-P; instead, it can be well reproduced as the explosion of a red supergiant for which the hydrogen-rich envelope is less than 1 $M_\odot$ (Nomoto et al. 1993; Podsiadlowski et al. 1993; Shigeyama et al. 1994; Bartunov et al. 1994; Utrobin 1994; Woosley et al. 1994; Young, Baron, & Branch 1995). The progenitor of SN 1993J is likely to have lost most of its H-rich envelope in a binary system, although a detailed evolutionary path to reach the presupernova configuration of SNe IIb is controversial; conservative mass transfer (Podsiadlowski et al. 1993; Ray, Singh, & Sutaria 1993; Woosley et al. 1994) and nonconservative transfer, i.e., merging with a small-mass companion star through common envelope evolution (Nomoto, Iwamoto, & Suzuki 1995; Nomoto et al. 1996) have been proposed.

Another important feature of SN 1993J is the mixing of the ejected material as inferred from observed spectra and photometry. Spectroscopically, the asymmetric profiles of the [O I] and [Mg I] emission lines at late times indicate mixing in the ejecta (Spyromilio 1994; Wang & Hu 1994). Shigeyama et al. (1994) first examined two extreme cases of mixing in their light curve modeling (i.e., with complete homogeneous mixing inside the helium layers and without mixing) and favored mixing of ^{56}Ni in SN 1993J. Woosley et al. (1994) also favored mixing of ^{56}Ni in their light curve modeling.

The occurrence of mixing and clumpiness in the supernova ejecta was first confirmed in SN 1987A. One clear confirmation is the early detection of hard X-rays and gamma-rays from the decays of ^{56}Ni and ^{56}Co (e.g., Kumagai et al. 1989), which is well modeled by mixing of ^{56}Ni into the outer envelope. Stimulated by these observations and theory, a number of multidimensional simulations have been performed to show that the Rayleigh-Taylor (R-T) instability indeed develops in the ejecta of SN 1987A (Arnett et al. 1989; Hachisu et al. 1990, 1992; Müller et al. 1991; Den, Yoshida, & Yamada 1990; Herant & Benz 1993). It was found that the instability is weak at the He/C+O and Ni/O interfaces but strong at the H/He interface, which can be expected from the large helium core mass ~ 6 $M_\odot$ and the massive hydrogen-rich envelope ~ 10 $M_\odot$. In other words, the penetration of ^{56}Ni into the hydrogen-rich envelope (and vice versa) occurs because the core materials are strongly decelerated by the massive hydrogen-rich envelope.

Such mixing can occur in other types of supernovae and provide interesting diagnostics of the internal structure of the progenitors. The extent of mixing and clumpiness affects the light curve and spectra. A number of hydrodynamical simulations have shown that the R-T instabilities arise in the Type II-P explosions of red supergiants (Herant & Woosley 1994; Shigeyama et al. 1996) as in SN 1987A and the helium star models of Type Ib supernovae (Hachisu et al. 1991, 1994).

These studies indicate the importance of multidimensional simulations of instabilities in supernova ejecta. This is particularly interesting for SN 1993J because its presupernova structure is thought to be quite different from other supernovae. Conversely, we may strongly constrain the

mass and structure of the progenitor because the R-T instabilities are sensitive to the density structure of the progenitor.

Despite the importance of these simulations, no such simulation has been conducted before. Therefore, we have carried out two-dimensional hydrodynamical simulations for the R-T instability in the ejecta of SN 1993J to examine the extent of mixing and the resultant abundance distributions quantitatively. In parallel, we have calculated bolometric light curves for several explosion models with various extents of mixing and compared them with the observations. These results enable us to constrain the masses of the helium core and the envelope of the progenitor.

If we can obtain a good estimate of the progenitor's main-sequence mass, it will be useful in understanding the still debated presupernova evolution and in providing nucleosynthesis yields as a function of stellar mass in combination with SN 1987A and possibly SN 1994I. The latter is possible because the Cepheid distance to SN 1993J has been measured as 3.63 Mpc with the *HST* (Freedman et al. 1993), with which good estimates of the masses of nucleosynthesis products such as Fe and O have been obtained (see § 3).

In the next section, the presupernova models for SN 1993J are described. Results of the linear stability analysis and the two-dimensional hydrodynamical simulations are shown in §§ 3 and 4, respectively. The effects of ^{56}Ni mixing on the optical light curve are discussed in § 5. Finally, we summarize some constraints on the explosion models.

2. HYDRODYNAMICAL MODELS

2.1. *Presupernova Models of the Progenitor*

The progenitor models are constructed following Shigeyama et al. (1994). We use the presupernova helium cores of masses $M_\alpha = 3.3\ M_\odot$ and $4\ M_\odot$ (Nomoto & Hashimoto 1988), which are evolved from the main-sequence stars of $M_{ms} = 13\ M_\odot$ and $15\ M_\odot$, respectively. The adopted main-sequence masses are consistent with the inferred progenitor's luminosity (Wheeler & Filippenko 1995; Hashimoto, Iwamoto, & Nomoto 1993). For the H-rich envelope, we adopt several values of its mass ranging from $0.1\ M_\odot$ to $0.5\ M_\odot$. If the mass loss is due to a spiral-in of a small-mass companion star (Nomoto et al. 1995), then the remaining envelope mass depends on the companion's orbital energy available to eject the envelope material. The hydrostatic and thermal equilibrium H/He envelope models are constructed for various masses M_{env}, radii R_i, and the helium abundance Y to smoothly fit to the helium core. The model parameters are summarized in Table 1. The density distributions for 3H11, 3H41, 4H13, and 4H47 are shown in Figure 1.
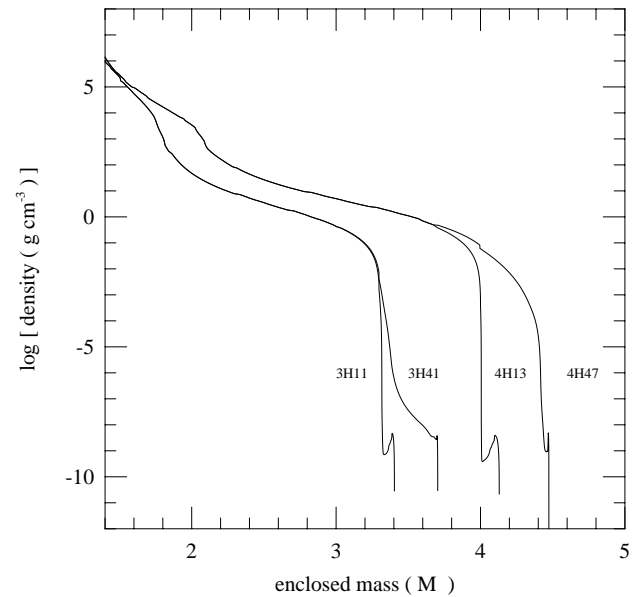

FIG. 1.—Density structures of the progenitor models at the onset of collapse.

These models have large helium abundances in the envelope. Such an enhancement of helium is expected from the gradient of helium abundance in the deepest layers of the envelope (see, e.g., Saio, Nomoto, & Kato 1988). If most of the hydrogen-rich envelope is removed, the helium-rich layer is exposed, as seen in Yamaoka & Nomoto (1991) and Nomoto, Kumagai, & Shigeyama (1991); they have calculated mass loss from the initially 13 $M_\odot$ star, which reduces the envelope mass down to 0.3 $M_\odot$ and enhances the average helium mass fraction up to ~ 0.5 at the termination of Roche lobe overflow (see also Woosley et al. 1994).

2.2. *Hydrodynamics of Explosion*

We simulate the core collapse-induced explosion by depositing thermal energy at the mass cut (a partition between neutron star and ejecta) generating a strong outward shock wave. The deposited energy is set to produce the kinetic energy of explosion $E = 1 \times 10^{51}$ ergs. The mass cut is chosen to produce 0.1 $M_\odot$ of ^{56}Ni, consistent with light curve calculations (see § 5). The propagation of the shock wave and hydrodynamics of the ejecta are calculated with a one-dimensional Lagrangian PPM code (Shigeyama et al. 1994). Nucleosynthesis yields behind the shock wave are nearly the same as obtained in the 3.3 $M_\odot$ and 4.0 $M_\odot$ He core models (Shigeyama & Nomoto 1990; Iwamoto 1994; Thielemann, Nomoto, & Hashimoto 1996).

Figures 2a and 2b show the evolution of the density and pressure profiles in the ejecta of 4H13 and 3H11, respec-

TABLE 1

PARAMETERS FOR PROGENITOR MODELS OF SN 1993J

Name	$M_{env}/M_\odot$	$M_{ej}/M_\odot$	$M_{Ni}/M_\odot$	$R_i/R_\odot$	$L/L_\odot$	Y	E_{exp} $(10^{51}$ ergs$)$
3H11......	0.11	2.06	0.1	450	4.1×10^4	0.54	1.0
3H41......	0.41	2.36	0.1	450	4.1×10^4	0.54	1.0
4H13......	0.13	2.78	0.1	580	6.8×10^4	0.56	1.0
4H47......	0.47	3.12	0.1	350	6.8×10^4	0.79	1.0

NOTE.—M_{env}, envelope mass; M_{ej}, total ejecta mass; M_{Ni}, ^{56}Ni mass. R_i are the initial radii, L is the presupernova luminosity, and Y is the helium mass fraction in the envelope.
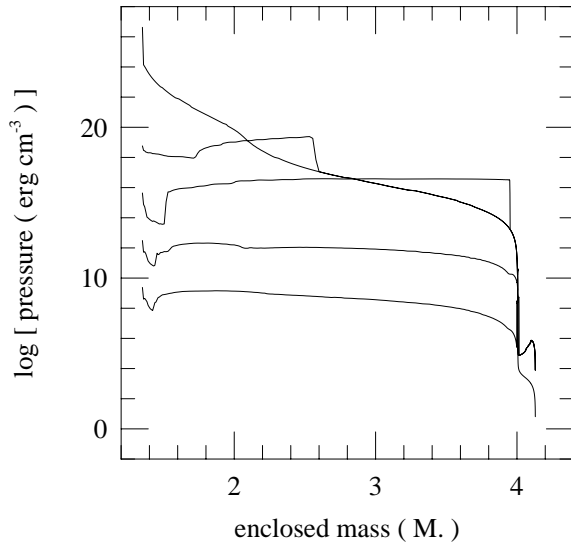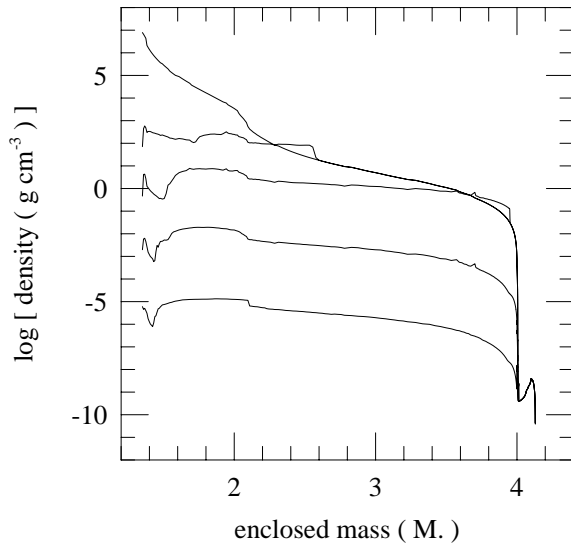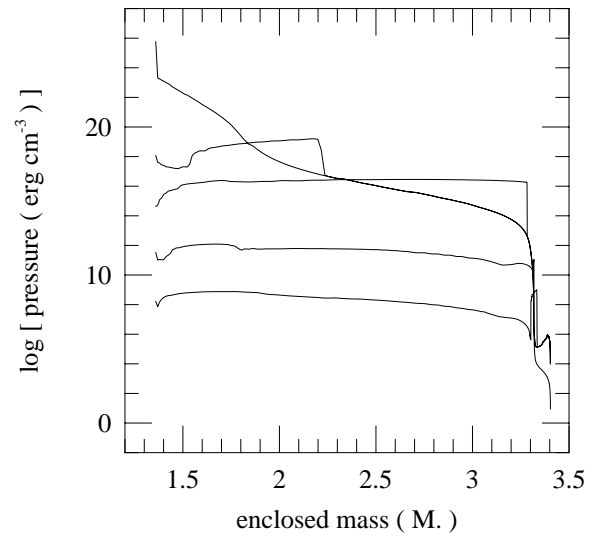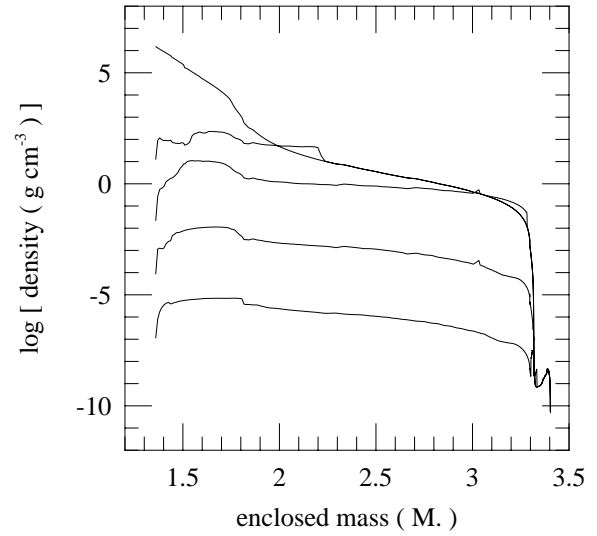
FIG. 2a

FIG. 2b

FIG. 2.—Density and pressure profiles for (a) 4H13 and (b) 3H11 after the explosion, at (from top to bottom) 0, 10, 100, 1000, and 10,000 s

tively. When the shock wave passes through the He/C+O interface, the ejecta behind the shock front undergoes a strong deceleration, which forms an inwardly propagating reverse shock. This stage corresponds to the profiles at $t = 10$ s in Figures 2a and 2b. Between the two shock waves, there appears a region with pressure inversion. The R-T instability is expected to arise at the interface that is due to the opposite signs of the density and pressure gradients. When the shock wave arrives at the H/He interface, it is strongly decelerated again in the same manner as it passed the He/C+O interface. This is shown in the profiles at $t = 1000$ s in Figures 2a and 2b.

This complicated behavior of hydrodynamics, the alternate acceleration and deceleration, can be explained by behavior of the self-similar solutions of the blast shock in spherically expanding gas with a power-law density distribution $\rho \propto r^{-n}$ (Sedov 1959; Chevalier 1976). In these solutions, the forward shock wave is accelerated for $n > 3$, while the shock is decelerated for $n < 3$ (Müller et al. 1989; Herant & Woosley 1994). Figure 3 shows ρr^3 against the

enclosed mass M_r for the initial density profiles of 4H13 and 3H11. It is seen that there are two distinct regions where the shock wave should be decelerated and the R-T instability would grow.

3. LINEAR STABILITY ANALYSIS

In this section, we present an estimate of the R-T growth by the linear stability analysis. Our method is basically the same as that used for SN 1987A by Ebisuzaki, Shigeyama, & Nomoto (1989), Benz & Thielemann (1991), and Müller et al. (1991). In the classical case in which two homogeneous fluids are stratified in the gravitational field, a linear growth rate is given as (Chandrasekhar 1981)

$$G_{\rm RT}^2 = \frac{\rho_+ - \rho_-}{\rho_+ + \rho_-}\, kg \, , \qquad (1)$$

where ρ_+ and ρ_- are the densities in the upper and lower layers, respectively, k is the wavenumber of the perturbation, and g is the acceleration due to the gravity. This
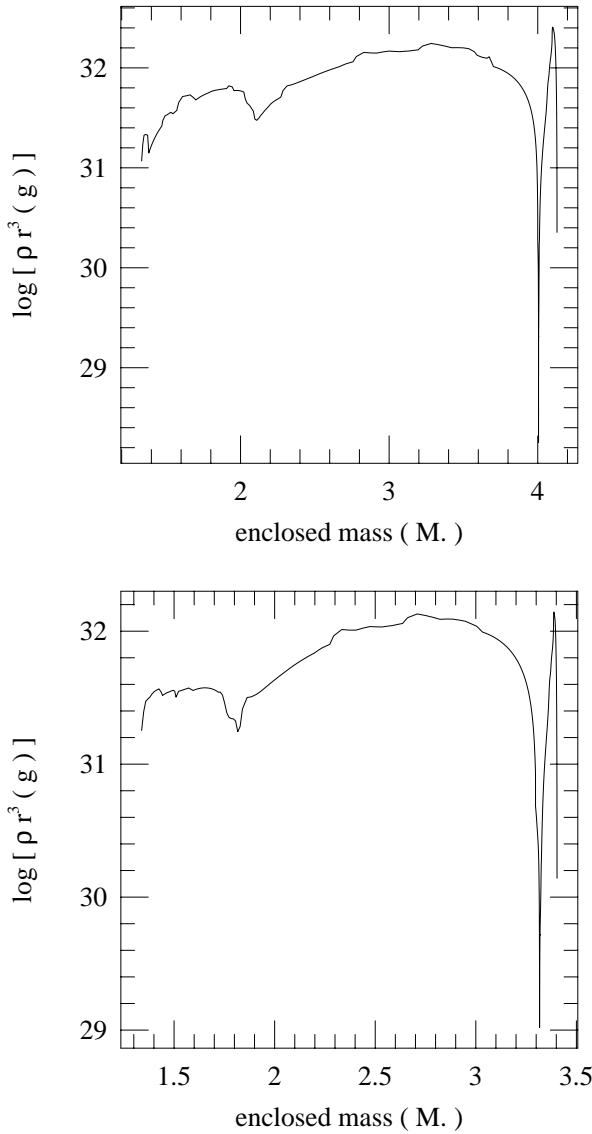
FIG. 3.—Plots of ρr^3 against enclosed mass $M_r/M_\odot$ for 4H13 (upper) and 3H11 (lower).

formula can be applied to the shocked ejecta of a supernova by replacing g with the effective gravity g_{eff} defined as

$$g_{eff} = -g - \frac{1}{\rho}\frac{dP}{dr} \simeq -\frac{1}{\rho}\frac{dP}{dr}. \tag{2}$$

The pressure gradient term dominates in the strongly decelerated blast wave, and the stellar gravity is negligibly small in the expanding ejecta. Equations (1) and (2) show that the ejecta becomes R-T unstable if the density and pressure gradients have opposite signs,

$$\frac{dP}{dr}\frac{d\rho}{dr} < 0. \tag{3}$$

We calculate the growth factor of the amplitude at each layer, ζ/ζ_0, by integrating the growth rate at each stage of spherically symmetric explosion models as

$$\frac{\zeta}{\zeta_0} = \exp\left\{\int_0^t \mathrm{Re}\,[G_{RT}(t')]dt'\right\}, \tag{4}$$

where ζ_0 is the initial amplitude of the perturbation and $\mathrm{Re}\,(G_{RT})$ indicates the real part of the growth rate. As a linear growth rate, we take that of the fastest growing mode with the wavelength of about pressure scale height. The formula of the growth rate for the continuous density distribution (Chandrasekhar 1981) reduces to the following expression based on the above assumption:

$$G_{RT}^2 \simeq -\frac{1}{\gamma}\frac{c_s^2}{1+\pi^2}\frac{1}{H_\rho H_P}. \tag{5}$$

Here γ is the adiabatic index, c_s is the adiabatic sound velocity, and H_ρ and H_P are the density and pressure scale heights, respectively, which are defined as

$$H_\rho = \frac{dr}{d\ln\rho}, \quad H_P = \frac{dr}{d\ln P}. \tag{6}$$

Note that the linear stability analysis is not valid after the instability develops into the nonlinear phase. However, it is still meaningful to see qualitatively which regions of the ejecta are unstable. We calculate the R-T growth by equation (4) in parallel with one-dimensional hydrodynamical simulations. Figure 4a shows the amplitude ζ/ζ_0 versus enclosed mass for both 3H41 and 4H47 at $t = 1$ day after the explosion.

There appear three distinct unstable regions: (1) the He/C + O interface around $M_r = 1.8\ M_\odot$ (3H41) and 2.1 $M_\odot$ (4H47); (2) the H/He interface around $M_r = 3.3\ M_\odot$ (3H41) and 4.0 $M_\odot$ (4H47); (3) the surface region near the density inversion as seen in Figure 1. These regions are coincident with those expected from the behavior of ρr^3 in Figure 3. For 3H11 and 4H13, models with a smaller mass envelope, the growth is almost the same as for 3H41 and 4H47, respectively, but is slightly different due to the different envelope structure (Fig. 4b).

Figures 4a and 4b also show that at the He/C + O interface the growth is somewhat larger for 3H models than for 4H models. This is because the mass ratio between the He layer and the C-Ni core is larger in the 3.3 $M_\odot$ He core than in the 4 $M_\odot$ core, producing a larger deceleration in the C-Ni core (Hachisu et al. 1991).

4. TWO-DIMENSIONAL SIMULATIONS

We carry out two-dimensional hydrodynamical simulations to follow the nonlinear growth of the R-T instabilities and mixing. The linear stability analysis indicates that the instability would grow in some particular regions, i.e, at the He/C + O interface, the H/He interface, and near the surface. The radius at the He/C + O interface is about ~ 1 $R_\odot$ for both progenitor models, being 2 orders of magnitude smaller than that of the H/He interface. When the shock wave reaches the H/He interface, the instability at the He/C + O interface has already ceased to grow. For these reasons, we examine the instabilities in the He core and near the core/envelope boundary in separate calculations to avoid a significant numerical diffusion that is due to unnecessary rezoning.

Our hydrodynamical code is a standard third-order TVD (total variation diminishing) scheme with a preprocessing flux limiter using the Roe's approximate Riemann solver (Hachisu et al. 1992, 1994). It has second-order accuracy in time by using two-step time integration. We make several improvements in treating the advection of the chemical composition of the fluid. The advection equations of the
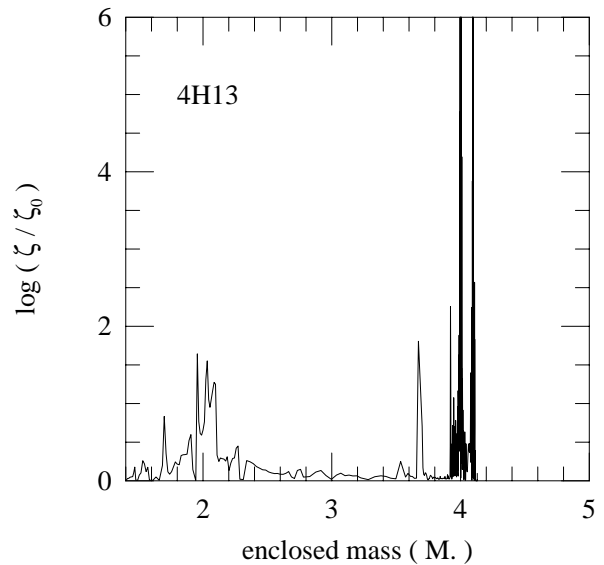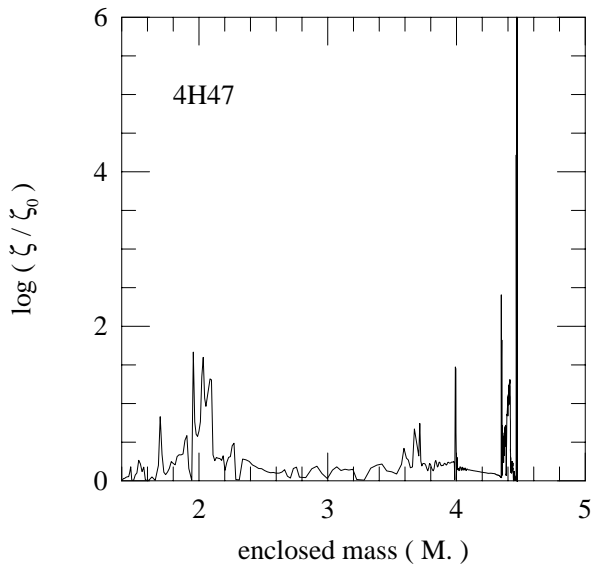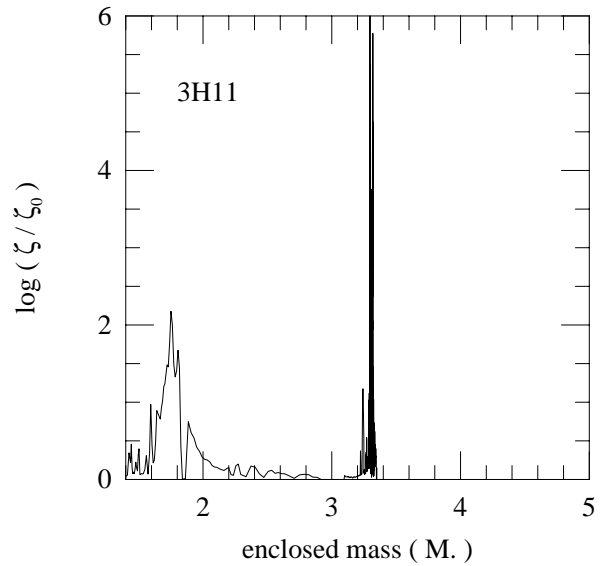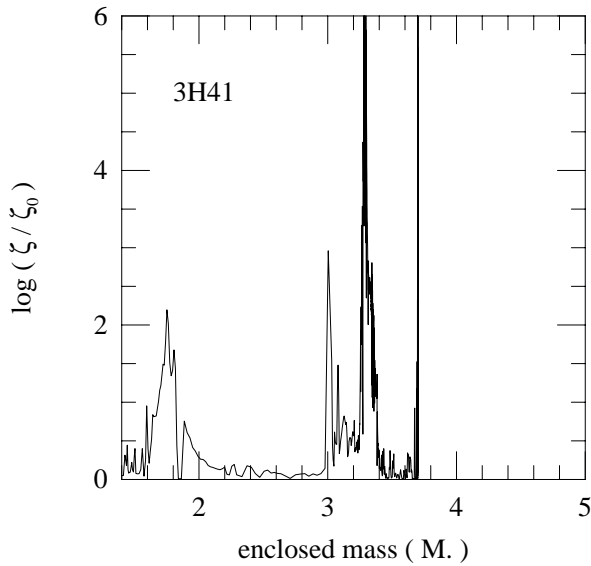
FIG. 4a

FIG. 4b

FIG. 4.—Rayleigh-Taylor growth as a function of enclosed mass $M_r/M_\odot$ (a) for 3H41 (*upper*) and 4H47 (*lower*), and (b) for 3H11 (*upper*) and 4H13 (*lower*)

mass fractions are solved as parts of the extended Roe matrix, which enables us to treat them consistently with the Euler equations constraining the sum of the mass fractions to be unity. This new method is advantageous for accurately calculating the extent of mixing. We use an equation of state with a constant adiabatic index 4/3, which is a good approximation since the ejecta remains in the radiation-dominant phase because of high temperatures. Nuclear burning during the shock propagation is not included in our two-dimensional code because the temperatures and densities of the ejecta are already too low when the two-dimensional simulations are started at $t = 10$ s after the explosion.

We use cylindrical coordinates with 513 grid points in each axis, R and Z. Several rezonings, 3 or 4 times for all runs, are still necessary despite the separate studies of the inner and outer parts. As the shock wave arrives at nearly the numerical boundaries, we double the mesh size and remap all the flow variables onto the new grid system. Each physical quantity $q(2i - 1, 2j - 1)$ in the old grid is project-

ed to $q(i, j)$ in one-fourth of the new computational area. The initial profiles are inserted in the remaining part. The early shock propagations are simulated with a spherically symmetric one-dimensional hydrodynamics code (see § 2) until $t = 10$ s after the explosion when the flow is mapped onto the two-dimensional code. We apply random perturbations to the velocity field interior to the shock front (Hachisu et al. 1994) shortly after the shock has passed the relevant interface, at $t = 10$ s for the He/C + O interface and at $t = 300$–400 s for the H/He interface. The latitudinal angle is divided into n pieces, and the velocity field is perturbed in each area of π/n angles as

$$v_r = v_0 [\![1 + \epsilon\{2\,\mathrm{rmd}[(n\theta/\pi)] - 1\}]\!] , \quad v_\theta = 0 , \quad (7)$$

where v_0 is the spherically symmetric expansion velocity at $t = 10$ s taken from the one-dimensional calculation. We take $n = 20$ in all cases. The symbol rmd(i; integer) denotes a sequence of uniform random numbers ranging from 0 to 1 and $[x]$ denotes the maximum integer that cannot exceed x. Since the origin and the size of the initial perturbation is
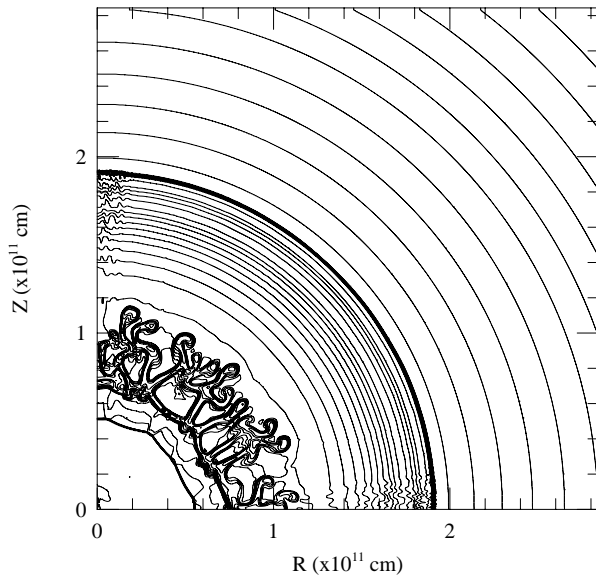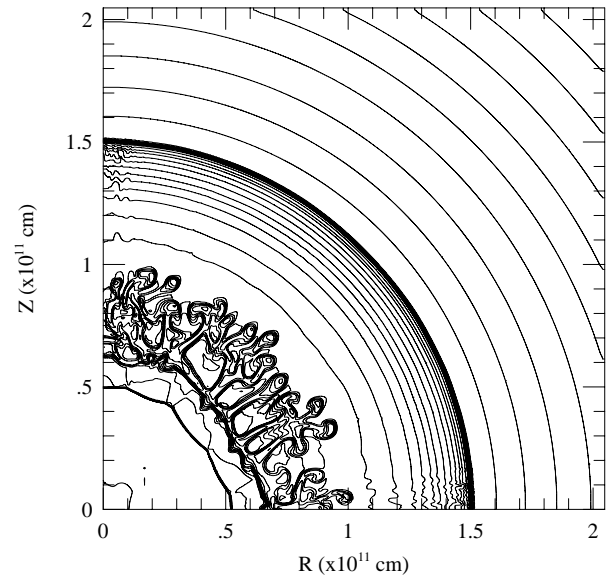
FIG. 5a

FIG. 5b

FIG. 5.—Density contours for (a) 3H41 (174 s) and (b) 4H47 (149 s)

highly uncertain, we take $\epsilon = 0.05$ in all cases. Such a relatively large perturbation may be realized if the convective motion during oxygen shell burning is as violent as simulated by Bazan & Arnett (1994). The extent of mixing was found to be nearly independent of both the mesh resolution and the size of the perturbations as long as the amplitude is larger than this value (Hachisu et al. 1992, 1994).

Figures 5a and 5b show the density contour near the He/C+O interface for 3H41 (at $t = 174$ s) and 4H47 (at $t = 149$ s), respectively. Each contour is drawn with a logarithmically equal interval. It is seen that mushroom-like fingers are developed in the He core. This clearly shows that the R-T instability has grown to its nonlinear stage and a large-scale mixing of the elements occurred in the velocity space within the He core.

Figures 6a and 6b show the density contour in the outer part near the H/He interface for 3H41 (at $t = 5.34 \times 10^4$ s) and 4H47 (at $t = 3.95 \times 10^4$ s), respectively. The R-T instability also grows as a result of the steep density gradient above the interface. However, the finger-like structures near the bottom of the H-rich envelope do not develop as much as in the inner core region, and thus the extent of mixing in the envelope is much smaller than in the core. This is due to the small hydrogen-rich envelope mass and thus a weak deceleration.

We calculate averaged radial distributions of the chemical compositions in the ejecta from the results of the two-dimensional simulations. Figures 7 and 8 show the resultant abundance distributions against M_r for 3H41 and 4H47, respectively. It is seen that ^{56}Ni is mixed out to $M_r = 1.0$
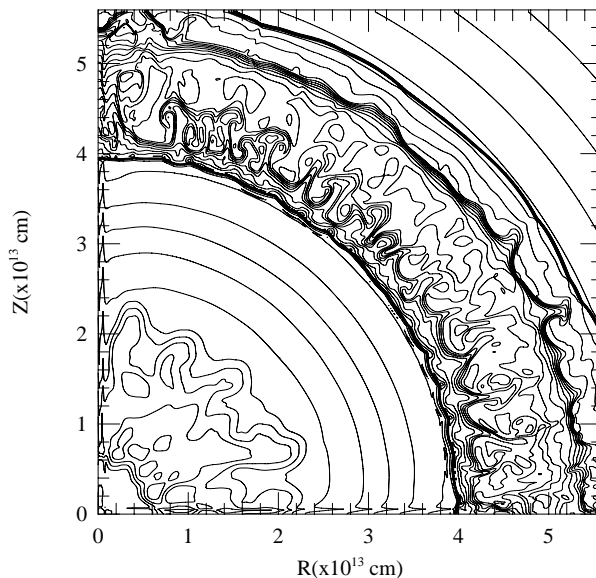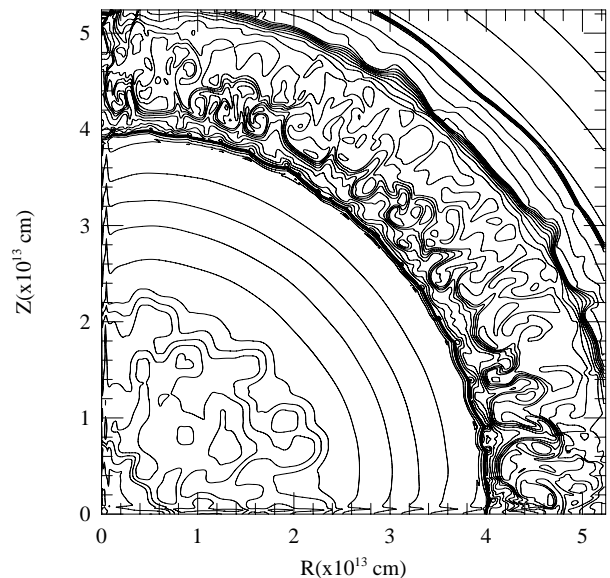

FIG. 6a

FIG. 6b

FIG. 6.—Density contours for (a) 3H41 (5.34×10^4 s) and (b) 4H47 (3.95×10^4 s)
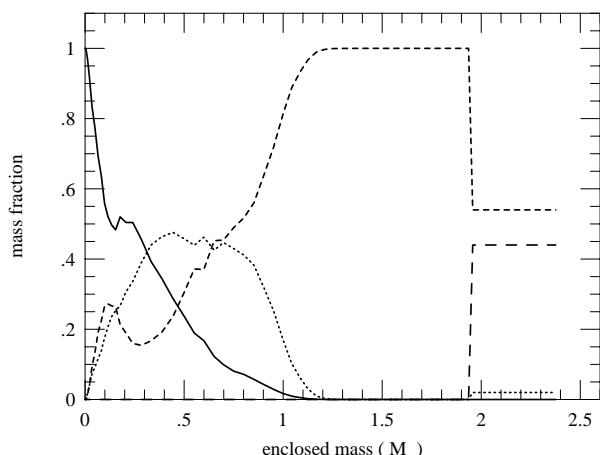
FIG. 7.—Averaged radial distribution of several elements as a function of M_r measured from the bottom of the ejecta for 3H41. Shown are the mass fractions of ^{56}Ni (*solid*), C+O (*dotted*), He (*dashed*), and H (*long-dashed*).

$M_\odot$ for 3H41 but only to $M_r = 0.5\ M_\odot$ for 4H47. Mixing of carbon and oxygen into the He layer is significant for both cases. Hydrogen is not significantly mixed down to the He core for both cases because of the small envelope mass. If the mass of the hydrogen-rich envelope is smaller (as in 3H11 and 4H13 in Table 1), the expanding core undergoes smaller deceleration so that the velocities of H, He, O, and Fe would be higher. Comparisons of the observed expansion velocities of H, He, O, and Fe with those predicted by the models will be made in § 6.

How the degree of mixing depends on the structure of the progenitors, in particular, the masses of the core and the envelope, can be understood from the linear stability analysis in § 3. In fact, with the two-dimensional hydrodynamical simulations of the R-T instabilities for SN 1987A and Type Ib supernovae, Hachisu et al. (1990, 1991, 1994) have shown that the R-T growth near the He/C+O interface in the core tends to be larger for a smaller mass He core.

With these studies, the differences between SN 1993J and SN 1987A can be summarized as follows. For SN 1987A, the large-scale mixing is induced mostly by the R-T insta-

bility near the H/He interface, while the mixing around the He/C+O interface is not significant. For SN 1993J, in contrast, the R-T instability at the H/He interface is much weaker than in SN 1987A because of the smaller envelope mass, while the He/C+O interface is the most unstable region and a large-scale mixing is induced in the He core.

5. OPTICAL LIGHT CURVE AND MIXING

As described in § 1, the optical light curve of SN 1993J showed a unique behavior, with neither a clear plateau nor a monotonic decline. It rapidly declined after the first maximum, then rose to the second peak in 10–15 days, and finally followed by a gradually declining tail. The basic feature of this peculiar light curve can be accounted for with the Type IIb model, namely, the explosion of a red supergiant for which the hydrogen-rich envelope is quite thin.

The light curve analysis of SN1993J has shown that the progenitor radius and mass are the main parameters that determine the shape of the light curve (see, e.g., Shigeyama et al. 1994; Woosley et al. 1994; Young, Baron, & Branch 1995). These studies have also noted some effects of ^{56}Ni mixing on the light curve shape. In the earlier sections, we have shown that ^{56}Ni is indeed mixed into the He layer but that the degree of mixing depends on the progenitor's mass. Here we present a more detailed study of the optical light curve in order to determine the amount of mixing of ^{56}Ni and examine whether the plausible model for SN 1993J can be identified. More details, as well as the dependence on other parameters, will be presented in Young et al. (1996).

We calculate bolometric light curves for 3H11, 3H41, and 4H47 with several changes in the ^{56}Ni distribution. The light curve code is the same as used in Young et al. (1995), which is the flux-limited radiative transfer code assuming LTE. Figures 9–11 compare the theoretical light curves of these models with the observed bolometric light curve (Richmond et al. 1994; Lewis et al. 1994) with a distance to M81 of 3.63 Mpc (Freedman et al. 1994). In each of the figures, three degrees of mixing are used; for example, "Mix 0.2 $M_\odot$" implies that ^{56}Ni is uniformly mixed from the center to $M_r = 0.2\ M_\odot$. The explosion energy and ^{56}Ni masses are held at $E = 1 \times 10^{51}$ ergs and 0.1 $M_\odot$, respectively, for all the models.

The first peak in the light curve is produced by the radiation field established in the shock-heated H/He envelope, while the second peak is formed by diffusive leak of the deposited energy that is due to the radioactive decay of ^{56}Ni and ^{56}Co. Finally, the light curve enters an exponential declining tail that is due to the ^{56}Co decay.

The most obvious feature that the mixing affects is the tail of the light curve. The declining rate of the tail is faster for more extensive mixing and for a smaller mass He core, since the ejecta is more transparent to γ-rays. The no-mixing case for 3H11 has a brighter tail and a shallower slope than the observations. On the contrary, mixing to 1.0–1.5 $M_\odot$ for 3H41 gives a tail that is too steep to be compatible with observations.

The effects of mixing on the light curve shape around the dip at day 20 and the second peak are also seen. With more extensive mixing, the heating effect of radioactive decays starts to appear earlier so that the dip is shallower and the second peak is reached earlier. These effects are relatively small for 3H11 but are much more important for 3H41 and 4H47 because of the thicker envelope. For 3H41 a critical mixing mass is found to extend to $M_r = 1\ M_\odot$, at which the
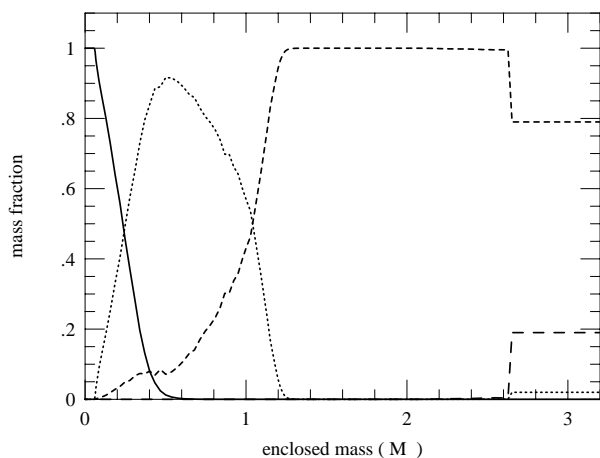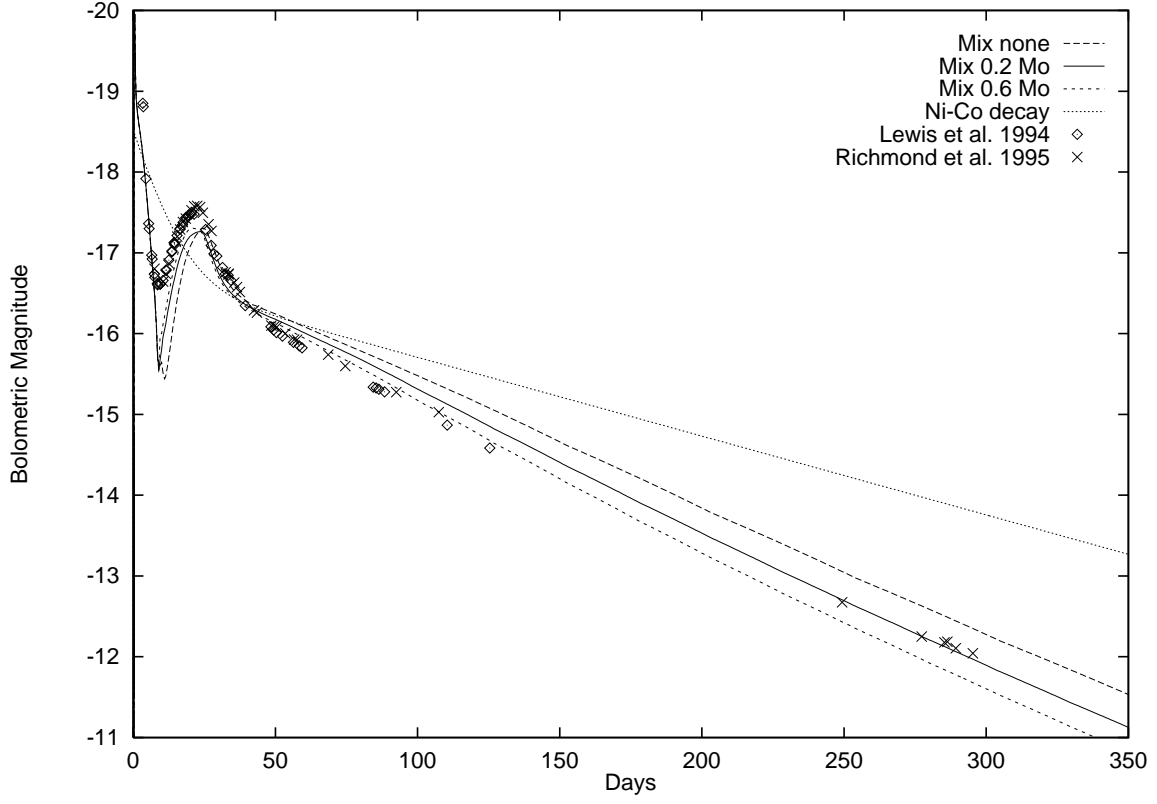

FIG. 8.—Same as Fig. 7, but for 4H47

Fig. 9.—Calculated bolometric light curves for 3H11 as compared with the observations of SN 1993J. From top to bottom, the dotted line shows the total energy deposition rate from the Ni-Co decay. Other three lines show the results with different degrees of mixing: no mixing (*long-dashed*), mix 0.2 $M_\odot$ (*solid*), and mix 0.6 $M_\odot$ (*short-dashed*). Here "mix 0.2 $M_\odot$," for example, means that ^{56}Ni is uniformly mixed from the center to $M_r = 0.2\ M_\odot$. The solid line (mix 0.2 $M_\odot$) gives the best fit to the observations by Lewis et al. (1994) (*diamond*) and Richmond et al. (1995) (*cross*).
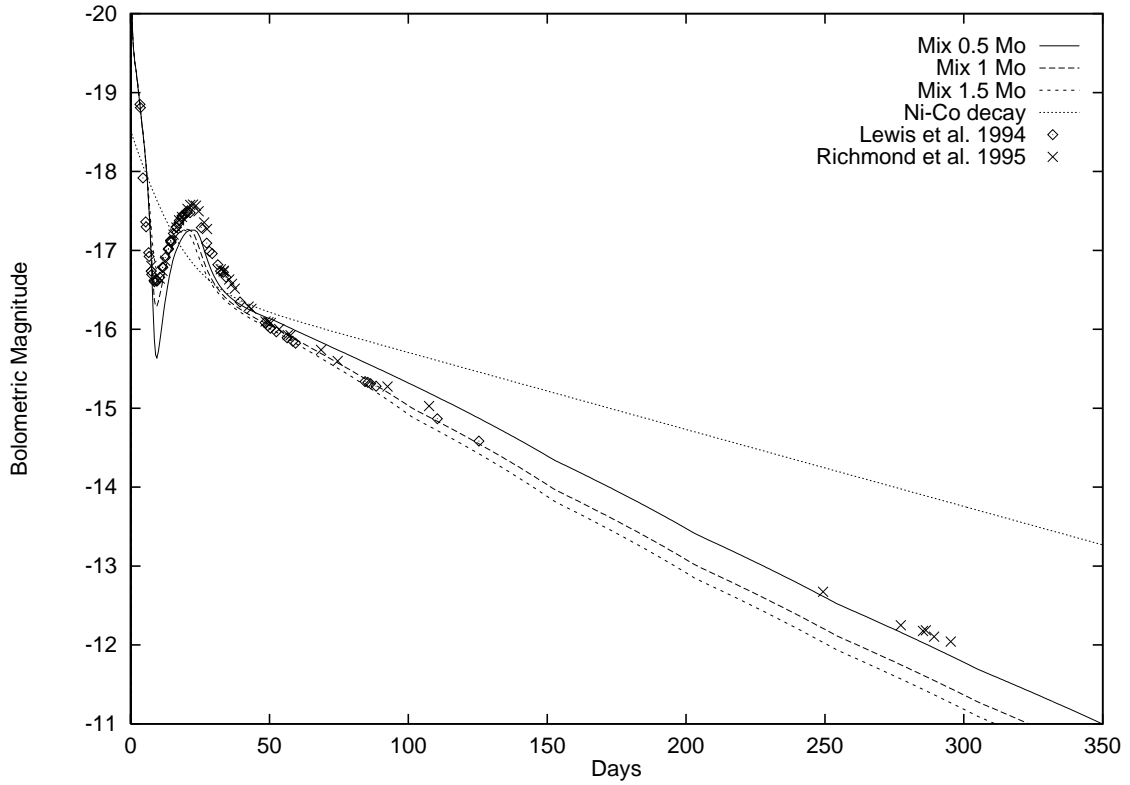

Fig. 10.—Same as Fig. 9, but for 3H41 with three different degrees of mixing: mix 0.5 $M_\odot$ (*solid*), mix 1 $M_\odot$ (*long-dashed*), and mix 1.5
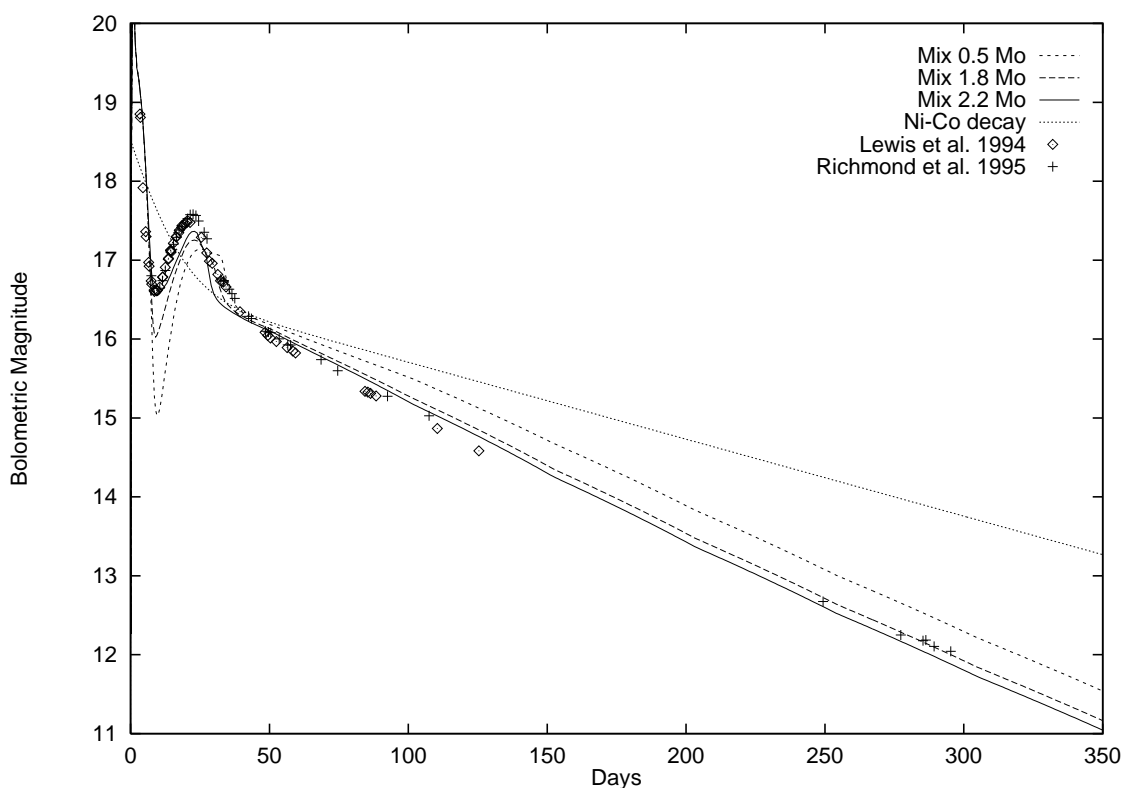
FIG. 11.—Same as Fig. 9, but for 4H47 with three different degrees of mixing: mix 0.5 $M_\odot$ (short-dashed), mix 1.8 $M_\odot$ (long-dashed), and mix 2.2 $M_\odot$ (solid) from high- to low-luminosity tail.

fit at day 20 is improved. However, mixing to this extent gives a tail that is too steep, as is seen in Figure 10. For 4H47, the tail is reproduced well with the mixing up to 1.8–2.2 $M_\odot$, and the mixing out to 2.2 $M_\odot$ gives a good fit to the dip at day 20.

To summarize, the observed light curve shape around the dip, the second peak, and its tail are well reproduced with the model 4H47 if the mixing of ^{56}Ni extends to $M_r \sim 2$ $M_\odot$. For 3H11 and 3H41, the mixing produces a better fit to the tail (solid line) but tends to form a dip at day 20. Improvement of the radiative transfer code might improve the fit of the early light curve. However, the luminosity on the tail depends only on the gamma-ray opacity and is not expected to change.

6. DISCUSSION

We compare the calculated abundance distributions as a function of M_r (measured from the bottom of the ejecta) (Figs. 7 and 8) and the expansion velocity (Figs. 12–15) with the degree of mixing required from the light curve modeling and the spectroscopic observations of SN 1993J.

After the expansion becomes homologous ($v \propto r$), the expansion velocity of each layer remains constant so that it can be directly compared with the observed velocities of various elements. In the hydrodynamical models, the expansion velocity v_{exp} depends on the explosion energy E_{exp} and the total mass of the ejecta M_{ej} as

$$v_{exp} \propto E_{exp}^{1/2} M_{ej}^{-1/2} . \qquad (8)$$

We have tried another two-dimensional simulation for 3H41 with a different explosion energy of $E_{exp} = 0.6 \times 10^{51}$ ergs and found little difference in the degree of mixing in the

M_r space compared with the case of $E_{exp} = 1.0 \times 10^{51}$ ergs. Therefore, we can safely assume that the velocity of each element in our models scales to the explosion energy as in equation (8).

Houck & Fransson (1996) have analyzed the spectra of SN 1993J and found that the observed spectra are well reproduced by their synthetic spectra if (1) some iron extends to at least 3000 km s^{-1} in the velocity space, (2) $\sim$0.5 $M_\odot$ oxygen occupies 1000—4000 km s^{-1}, and (3) the bulk of the hydrogen lies between 8500–10,000 km s^{-1}. For the hydrogen velocity, however, the minimum velocity has been determined to be $v_{H_{min}} \sim 7500$ km s^{-1} from the inner
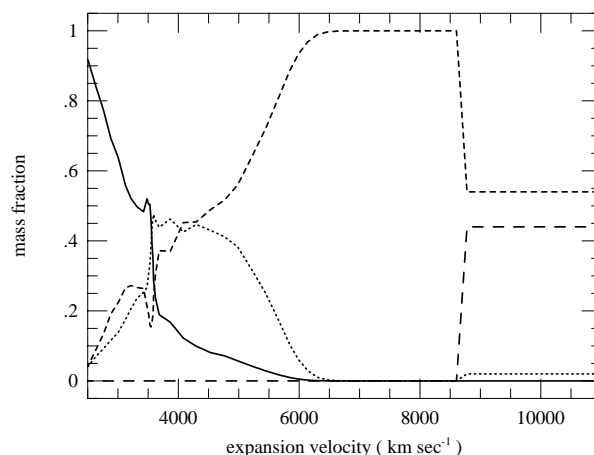

FIG. 12.—Averaged radial distribution of several elements as a function of the expansion velocity for 3H11. Shown are the mass fractions of ^{56}Ni (solid), C+O (dotted), He (dashed), and H (long-dashed).
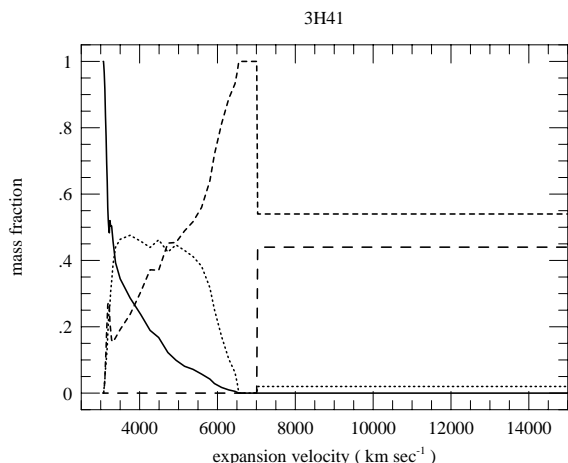
3H41

FIG. 13.—Same as Fig. 12, but for 3H41

edge of the Hα line profile at late times (Patat, Chugai, & Mazzali 1995).

The coexistence of oxygen and iron at 1000–3000 km s^{-1} implies the mixing of O and Fe in the velocity space, if O
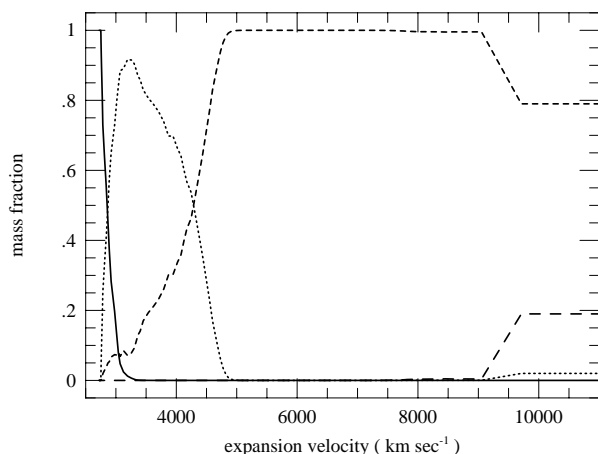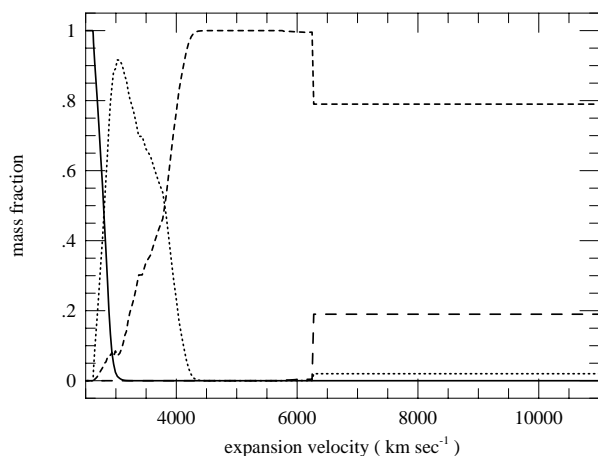

FIG. 14.—Same as Fig. 12, but for 4H13

FIG. 15.—Same as Fig. 12, but for 4H47

and Fe are separated at first. Our calculations show that even the larger mass 3H model, 3H41, has the maximum velocity of oxygen as high as 6500 km s^{-1}. Thus, considering the oxygen velocity, the 3H models are not preferable. The maximum velocity of oxygen in 4H47 is ∼4300 km s^{-1}, which is relatively agreeable.

The maximum velocity of ^{56}Ni (decaying eventually to Fe) is sensitive to the He core mass, i.e., $v_{Ni} \sim 6000$ km s^{-1} for 3H models and 3000 km s^{-1} for 4H models. This is because the He core with a smaller mass expands faster and undergoes more extensive mixing as discussed in § 3. Compared with the observations, v_{Ni} in 3H models is too fast. In 4H models, $v_{Ni} \sim 3000$ km s^{-1} is marginally acceptable but a little too low.

The minimum velocity of hydrogen, $v_{H_{min}}$, depends mainly on the mass of the H/He envelope, since the effect of mixing at the core/envelope boundary is not significant. For 3H11 (3H41) and 4H13 (4H47), $v_{H_{min}} \sim 8500$ (7000) km s^{-1} and 9000 (6300) km s^{-1}, respectively. Thus, if we adopt $v_{H_{min}} \sim 7500$ km s^{-1} from the late-time Hα profile, the envelope mass of ∼0.3–0.4 $M_\odot$ would be more consistent with the observed hydrogen velocities than ∼0.1 $M_\odot$.

We find in § 4 that the calculated light curves give the best fit to the observations if ^{56}Ni is mixed up to $M_r \sim 2.2~M_\odot$ for 4H47 and to 0.5–1.5 $M_\odot$ for 3H41 and 3H11. However, in our simulations of the R-T instabilities, ^{56}Ni is mixed up to $M_r \sim 0.5~M_\odot$ for 4H models and to 1.0 $M_\odot$ for 3H models. Thus, the calculated degree of ^{56}Ni mixing is too small in 4H models, while it is consistent with the light curve modeling in 3H models. We should note, however, that the agreement between the calculated and observed light curves is better for 4H47 than for 3H41.

The determination of oxygen mass from the late-time spectra would be another way to determine the progenitor's mass. Houck & Fransson (1996) estimated that the oxygen mass is ∼0.5 $M_\odot$. In the explosion models, the produced oxygen masses are 0.21, 0.42, and 1.5 $M_\odot$ for the He cores of 3.3, 4, and 6 $M_\odot$, respectively (Thielemann et al. 1996). Thus the 4 $M_\odot$ core model gives the more consistent oxygen mass.

The inconsistencies of the mixing in the 3H and 4H models with the spectroscopic and photometric observations can be reconciled as follows.

1. For 3H models, the fast decline of the tail may be improved if the explosion energy is as low as 0.8×10^{51} ergs. This is also suggested from the X-ray light curve analysis (Suzuki & Nomoto 1995).

2. For 4H models, to be consistent with the observed light curve, the mixing of ^{56}Ni should be much more extensive than that occurs in the 2D simulation. Such a large scale mixing would require an extremely large initial perturbations, which might be due to the neutrino-induced R-T instabilities (Herant, Benz, & Colgate 1992; Burrows, Hayes, & Fryxell 1995; Janka & Müller 1996), the convective oxygen shell burning just before the collapse (Bazan & Arnett 1994), or the spiral-in of a companion star in the common envelope scenario (Nomoto et al. 1995, 1996).

The instabilities in the H-rich envelope might be more extensive than our models show. An additional perturbation, such as an asymmetric structure (Höflich 1995) that is due to the spiral-in of the companion star into the envelope (Nomoto et al. 1995, 1996), would cause more mixing. It is important to know whether the density dis-

tribution in the H-rich envelope is largely changed as a result of the possible development of the above instabilities because the X-ray light curves (Zimmermann et al. 1994; Kohmura et al. 1994) has been found to be sensitive to the envelope structure of the ejecta (Suzuki & Nomoto 1995; Fransson, Lundqvist, & Chevalier 1996).

7. CONCLUSIONS

We have investigated the Rayleigh-Taylor instabilities in the ejecta of SN 1993J with a linear analysis of spherically symmetric explosion models and with a two-dimensional hydrodynamical simulations. We find the following conclusions:

1. The instability at the He/C+O interface develops to induce a large-scale mixing because of the relatively small He core mass.

2. The instability at the H/He interface is weak because of the small hydrogen-rich envelope mass.

Features (1) and (2) are in contrast to SN 1987A , which had the more massive He core and H envelope. The extent of mixing of heavy elements (Ni and C+O) is sensitive to the core mass. For the smaller core mass, the R-T instability is stronger and causes more extensive mixing as a result of the smaller mass ratio between the core and the He layer.

3. The optical light curves are calculated with a parameterized degree of mixing. The observed light curve is well reproduced if substantial amount of ^{56}Ni mixing occurs.

4. The calculated abundance distributions of the ejecta against the expansion velocity are compared with the observed velocities of Ni, O, and H. The model with the 3.3 $M_\odot$ He core and the hydrogen-rich envelope of 0.3–0.4 $M_\odot$ can well reproduce the observational feature of SN 1993J if the explosion energy is as low as $\sim 0.8 \times 10^{51}$ ergs. The model with the 4 $M_\odot$ He core and the $\sim 0.5 M_\odot$ envelope is also a good alternative if ^{56}Ni is more extensively mixed than our present calculations find, possibly as a result of much larger initial perturbations.

REFERENCES

Arnett, W. D., Fryxell, B. A., & Muller, E. 1989, ApJ, 341, L63
Baron, E., Hauschildt, P. H., & Young, T. R. 1995, Phys. Rep., 256, 23
Bartunov, O. S., Blinnikov, S. I., Pavlyuk, N. N., & Tsvetkov, D. Yu. 1994, A&A, 281, L53
Bazan, G., & Arnett, P. 1994, ApJ, 433, L41
Benz, W., & Thielemann, F.-K. 1990, ApJ, 348, L17
Burrows, A., Hayes, J., & Fryxell, B. A. 1995, ApJ, 450, 830
Chandrasekhar, S. 1981, Hydrodynamic and Hydromagnetic Stability (New York: Dover)
Chevalier, R. A. 1976, ApJ, 207, 872
Den, M., Yoshida, T., & Yamada, Y. 1990, Progr. Theor. Phys., 83, 723
Ebisuzaki, T., Shigeyama, T., & Nomoto, K. 1989, ApJ, 344, L65
Filippenko, A. V., et al. 1992, AJ, 104, 1543
Fransson, C., Lundqvist, P., & Chevalier, R. A. 1996, ApJ, 461, 993
Freedman, W. L., et al. 1994, ApJ, 427, 628
Hachisu, I., Matsuda, T., Nomoto, K., & Shigeyama, T. 1990, ApJ, 358, L57
———. 1991, ApJ, 368, L27
———. 1992, ApJ, 390, 230
———. 1994, A&AS, 104, 341
Hashimoto, M., Iwamoto, K., & Nomoto, K. 1993, ApJ, 414, L105
Herant, M., & Benz, W. 1991, ApJ, 370, L81
Herant, M., Benz, W., & Colgate, S. 1992, ApJ, 395, 642
Herant, M., & Woosley, S. E. 1994, ApJ, 425, 814
Höflich, P. 1995, ApJ, 440, 821
Houck, M., & Fransson, S. 1996, ApJ, 456, 811
Iwamoto, K. 1994, M. A. thesis, University of Tokyo
Janka, H.-Th., & Müller, E. 1996, A&A, 306, 167
Kohmura, Y., et al. 1994, PASJ, 46, L157
Kumagai, S., Shigeyama, T., Nomoto, K., Itoh, M., Nishimura, J., & Tsuruta, S. 1989, ApJ, 345, 412
Lewis, J. R., et al. 1994, MNRAS, 266, L27
Müller, E., Fryxell, B. A., & Arnett, W. D. 1991, A&A, 251, 505
Müller, E., Hillebrandt, W., Orio, M., Höflich, P., Mönchmeyer, R., & Fryxell, B. A. 1989, A&A, 220, 167
Nomoto, K., & Hashimoto, M. 1988, Phys. Rep., 163, 13
Nomoto, K., Iwamoto, K., & Suzuki, T. 1995, Phys. Rep., 256, 173
Nomoto, K., Iwamoto, K., Suzuki, T., Pols, O. R., Yamaoka, H., Hashimoto, M., Höflich, P., & van den Heuvel, E. P. J. 1996, in IAU Symp. 165, Compact Stars in Binaries, ed. J. Paradij, E. P. J. van den Heuvel, & E. Kuulkers (Dordrecht: Kluwer), 119

Nomoto, K., Kumagai, S., & Shigeyama, T. 1991, in AIP Conf. Proc. 232, Gamma-Ray Line Astrophysics, ed. P. Durouchoux & N. Prantzos (New York: AIP), 236
Nomoto, K., Suzuki, T., Shigeyama, T., Kumagai, S., Yamaoka, H., & Saio, H. 1993, Nature, 364, 507
Patat, F., Chugai, N., & Mazzali, P. A. 1995, A&A, 299, 715
Podsiadlowski, Ph., Hsu, J. J. L., Joss, P. C., & Ross, R. R. 1993, Nature, 364, 509
Ray, A., Singh, P., & Sutaria, F. K. J. 1993, A&A, 14, 53
Richmond, M. W., Treffers, R. R., Filippenko, A. V., Piak, Y., Leibundgut, B., Schulman, E., & Cox, C. V. 1994, AJ, 107, 1022
Saio, H., Nomoto, K., & Kato, M. 1988, Nature, 334, 508
Schmidt, B., et al. 1993, Nature, 364, 600
Sedov, L. I. 1959, Similarity and Dimensional Methods in Mechanics (New York: Academic)
Shigeyama, T., Iwamoto, K., Hachisu, I., & Nomoto, K. 1996, in IAU Colloq. 145, Supernovae and Supernova Remnants, ed. R. McCray & Z. Wang (Cambridge: Cambridge University Press), 129
Shigeyama, T., & Nomoto, K. 1990, ApJ, 360, 242
Shigeyama, T., Suzuki, T., Kumagai, S., Nomoto, K., Saio, H., & Yamaoka, H. 1994, ApJ, 420, 341
Spyromilio, J. 1994, MNRAS, 266, 61
Suzuki, T., & Nomoto, K. 1995, ApJ, 455, 658
Thielemann, F.-K., Nomoto, K., & Hashimoto, M. 1996, ApJ, 460, 408
Utrobin, V. 1994, A&A, 281, L89
Wang, L., & Hu, J. Y. 1994, Nature, 369, 380
Wheeler, J. C., & Filippenko, A. V. 1995, in IAU Colloq. 145, Supernovae and Supernova Remnants, ed. R. McCray & Z. Wang (Cambridge: Cambridge University Press), 241
Woosley, S. E., Eastman, R. G., Weaver, T. A., & Pinto, P. A. 1994, ApJ, 429, 300
Yamaoka, H., & Nomoto, K. 1991, in ESO/EIPC Workshop, SN1987A and Other Supernovae, ed. I. J. Danziger & J. Kjär (Garching: ESO), 193
Young, T. R., Baron, E., & Branch, D. 1995, ApJ, 449, L51
Young, T. R., Nomoto, K., Shigeyama, T., & Iwamoto, K. 1996, in preparation
Zimmerman, H. U., et al. 1994, Nature, 367, 621